

ARTICLE OPEN

Magnetic domain engineering in SrRuO₃ thin films

Wenbo Wang^{1,6}, Lin Li^{2,3,6}, Junhua Liu², Binbin Chen³, Yaoyao Ji², Jun Wang³, Guanglei Cheng⁴, Yalin Lu⁵, Guus Rijnders³, Gertjan Koster³, Weida Wu¹ and Zhaoliang Liao¹✉

Magnetic domain engineering in ferromagnetic thin films is a very important route toward the rational design of spintronics and memory devices. Although the magnetic domain formation has been extensively studied, artificial control of magnetic domain remains challenging. Here, we present the control of magnetic domain formation in paradigmatic SrRuO₃/SrTiO₃ heterostructures via structural domain engineering. The formation of structural twin domains in SrRuO₃ films can be well controlled by breaking the SrTiO₃ substrate symmetry through engineering miscut direction. The combination of x-ray diffraction analysis of structural twin domains and magnetic imaging of reversal process demonstrates a one-to-one correspondence between structural domains and magnetic domains, which results in multi-step magnetization switching and anomalous Hall effect in films with twin domains. Our work sheds light on the control of the magnetic domain formation via structural domain engineering, which will pave a path toward desired properties and devices applications.

npj Quantum Materials (2020)5:73; <https://doi.org/10.1038/s41535-020-00275-5>

INTRODUCTION

A wide range of perovskite oxide heterostructures provide a fertile playground for discovering emergent properties owing to their diverse capabilities to tune delicate coupling between spin, charge, and orbital degrees of freedom^{1–3}. The two-dimensional electron/hole gas at LaAlO₃/SrTiO₃ interface^{4,5}, polar skyrmions in PbTiO₃/SrTiO₃ superlattice⁶, chiral spin fluctuation in 2D SrRuO₃ ferromagnet⁷ and the newly discovered infinite layer nickelate superconductor⁸ are just several remarkable examples out of many. Engineering the lattice structure through interfacial mismatch of lattice constant^{9–11} and symmetry^{12–14} is one key route toward desired electronic phases and functionalities. The key feature of the lattice of ABO₃ perovskite is the corners shared three-dimensional network of BO₆ octahedra where the lattice symmetry of a perovskite resides in. The rotation mode (in-phase, out-of-phase) and rotation amplitude of octahedra about the principle axes determine the lattice distortion and symmetry¹⁵. No matter what kinds of rotation patterns, they all share quite similar pseudocubic lattice with B site sitting in the center of oxygen octahedra and A site at the hole surrounded by eight octahedra to form ABO₃ stoichiometry. This structure character leads to easy and common formation of twin domains^{16–18}. Furthermore, mismatch of rotation mode and rotation amplitude, which is widely observed in many heterointerfaces, can also result in the formation of twin domains^{19,20}. Therefore, understanding the effect of twin domains is very crucial for perovskite heterostructures.

A lot of previous works have demonstrated the significant impact of domain walls on physical properties, such as local enhanced mobility of electron gas at LaAlO₃/SrTiO₃ interface by SrTiO₃ (STO) tetragonal domain wall^{16,21} and conductive ferroelectric domain walls in BiFeO₃ films^{22,23}. Given that many perovskites exhibit crystalline anisotropy, e.g., orthorhombic perovskite Pbnm^{11,12,24}, different domains in a film can exhibit quite different behaviors. As a result, a combined behavior from

different individual domains could lead to complex properties. However, it is challenging to identify the behavior of individual domains with microscopic size and to clarify their impacts on the global properties. How the individual domains affect the film properties remains an open question and requires further investigation.

In this letter, we explore the interplay between structural twin domains and transport/magnetic properties in epitaxial SrRuO₃ films grown on (001) SrTiO₃. The SrRuO₃ (SRO) is an important ferromagnetic metal widely used as oxide electrode materials in functional oxide heterostructures²⁴. The recent discoveries of topological Hall effect^{25–27}, chiral spin fluctuation⁷ and skyrmion^{27,28} bring the SRO back to the spotlight of condensed matter research. The SRO possesses orthorhombic structure (Pbnm) with $a = 5.56 \text{ \AA}$, $b = 5.53 \text{ \AA}$, and $c = 7.84 \text{ \AA}$ ²⁹. When SRO is epitaxially grown on (001) STO, the c -axis can lie either in-plane (along one of the two principal directions of STO) or out-of-plane, leading to six possible orthorhombic domains as shown in Fig. 1a. By controlling the formation of twin domains through breaking the STO fourfold symmetry via exposing either (010) or (100) facets at substrate step edge (see Fig. 1b), we found that the transport and magnetic properties are strongly influenced by domain structures. Different structural domains within the SRO films have different magnetization reversal behaviors, resulting in multiple-step anomalous Hall effect (AHE). By geometric control of the number of different types of magnetic domains in SRO films through tuning substrate terrace directions, the number of the plateaus in magnetization and AHE can be manipulated. These intriguing phenomena were directly visualized using cryogenic magnetic force microscopy (MFM). Moreover, domain formation affects the sign of magnetoresistance. Previous study shows that stripe-like domains induced by controlled thickness inhomogeneity along terrace edge can cause two-channel AHE³⁰. Our observation of terrace direction controlled structural inhomogeneity and thus multi-domain switching then further sheds the light on the crucial role of domain inhomogeneity in SRO

¹Department of Physics and Astronomy, Rutgers University, Piscataway, NJ, USA. ²National Synchrotron Radiation Laboratory, University of Science and Technology of China, Hefei, Anhui, China. ³MESA+ Institute for Nanotechnology, University of Twente, Enschede, the Netherlands. ⁴CAS Key Laboratory of Microscale Magnetic Resonance and Department of Modern Physics, University of Science and Technology of China, 230026 Hefei, China. ⁵Anhui Laboratory of Advanced Photon Science and Technology, University of Science and Technology of China, Hefei, China. ⁶These authors contributed equally: Wenbo Wang, Lin Li. ✉email: zliao@ustc.edu.cn

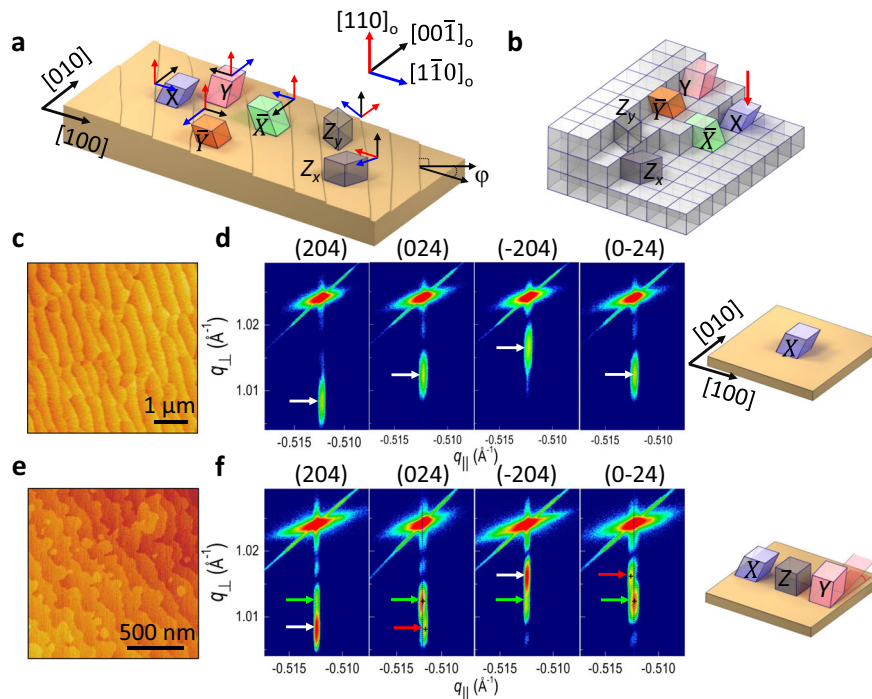


Fig. 1 Miscut direction controlled structural domain formation. **a** The six possible orthorhombic domains on a perovskite substrate. For X , \bar{X} , Y , and \bar{Y} domains, their $[00\bar{1}]_o$ lies in-plane and $[1\bar{1}0]_o$ are parallel to $[100]$, $[-100]$, $[010]$, and $[0\bar{1}0]$, respectively. The miscut direction is defined as φ . **b** The interface between STO unit cell and SRO unit cell of different domains. **c**, **e** Surface morphology of an SRO-15 and SRO-35, respectively. **d**, **f** RSMs of (204), (024), (-204) and (0-24) reflections for SRO-15 and SRO-35, respectively. The white and red arrows in **(f)** indicate peaks from X and Y -domains, respectively. The green arrows indicate $(44 \pm 4)_o$ from X and Y -domains, which are mixed with $(\pm 2 \pm 28)_o$ from Z -domain. The thicknesses of the films are 75 u.c.

transport and magnetic properties. What is more, the rational design of domain structures in perovskite heterostructures by growth symmetry breaking provides a smart route for properties and functionalities engineering.

RESULTS

Sample preparation

The SRO films were epitaxially grown on TiO_2 -terminated (001) STO substrates using pulsed laser deposition (PLD). The substrates were atomic flat with visible terraces and the terrace edges were unidirectional (see Supplementary Fig. 1). The miscut angles of STO substrates varied from 0.06 to 0.16° . The STO substrates had different miscut direction (φ), which is defined as the angle between terrace edges normal and $[100]$. A high oxygen partial pressure of 0.25 mBar was used for growth in order to minimize the oxygen off-stoichiometry and to favor a bulk like structure³¹. The growth of SRO films was in situ monitored by reflection high-energy electron diffraction (RHEED) and exhibited layer by layer growth mode at first few layers followed by step flow growth.

Due to the terrace structure where either (100) or (010) facets are exposed, different SRO orthorhombic domains have different characteristic vertical interfaces with STO at step edge. As a result, the growth symmetry is broken and a specific domain is more favored. The structures of vertical interface between SRO domains and STO are summarized in Fig. 1b. For convenience, the orthorhombic unit cell of SrRuO_3 is converted into pseudocubic unit cell by $[200] = [1\bar{1}0]_o$, $[020] = [00\bar{1}]_o$ and $[002] = [110]_o$ (see also Supplementary Fig. 2). Here, subscript 'o' refers to orthorhombic index. Due to $a \neq b$, the angle (β) between $[100]$ and $[001]$ is 89.26° rather than 90° (see Supplemental information in ref.¹⁹) This angle distinguishes the X from \bar{X} -domain when terrace direction is along STO $[010]$ direction. For X -domain, the (100) plane tilts away from the STO, whereas it tilts into the STO unit cell

for \bar{X} . Regarding Y and \bar{Y} -domain, their (100) planes though are both parallel to STO (100) plane, but their $[001]$ axes do not align to STO $[001]$. Similar situation occurs for both Z_x and Z_y -domains, which have misaligned principal axes with that of STO at (001) interface. For Z_x -domain, it has one more mismatch of inclined crystal plane with STO (100) plane. The different types of mismatch between the lattice of SRO domains and STO (inclined crystal planes angle vs. inclined crystal axes angle) break the growth symmetry, which shows that X -domain is more favored as illustrated below.

Miscut direction dependent domain structure

Impacts of terrace edge on domain formation are first examined by growing an SRO film on unidirectional terrace nearly along $[010]$ directions ($\varphi \approx 15^\circ$) as shown in Fig. 1c. For simplicity, SRO film with terrace direction φ is denoted as SRO- φ and the 15° unidirectional terrace SRO sample is then denoted as SRO-15. The thickness of this film is 75 unit cell. The orthorhombic domains were characterized by x-ray reciprocal space maps (RSMs) around (204) reflection of SRO film by azimuthally rotating the sample by 90° with respect to the surface's normal as shown in Fig. 1d. $\varphi = 0^\circ$ corresponds to $[100]$. The crystalline axes are intentionally defined in a way that the terrace ramping down direction is located in the first quadrant of coordination plane, which then allows us to identify the domain types and their relationship to terrace structures (see Supplementary Fig. 3). Due to the orthorhombic structure, six domains exhibit different diffraction patterns (see Supplementary Fig. 4). The downshift of (204) and upshift of (-204) with respect to (0 ± 24) peaks as shown in Fig. 1d suggest that the domain is X type. There are no visible impurity peaks, indicating single X -domain in SRO-15, consistent with the previous reports^{32–35}. In sharp contrast, evident two groups of reflection peaks from two domains

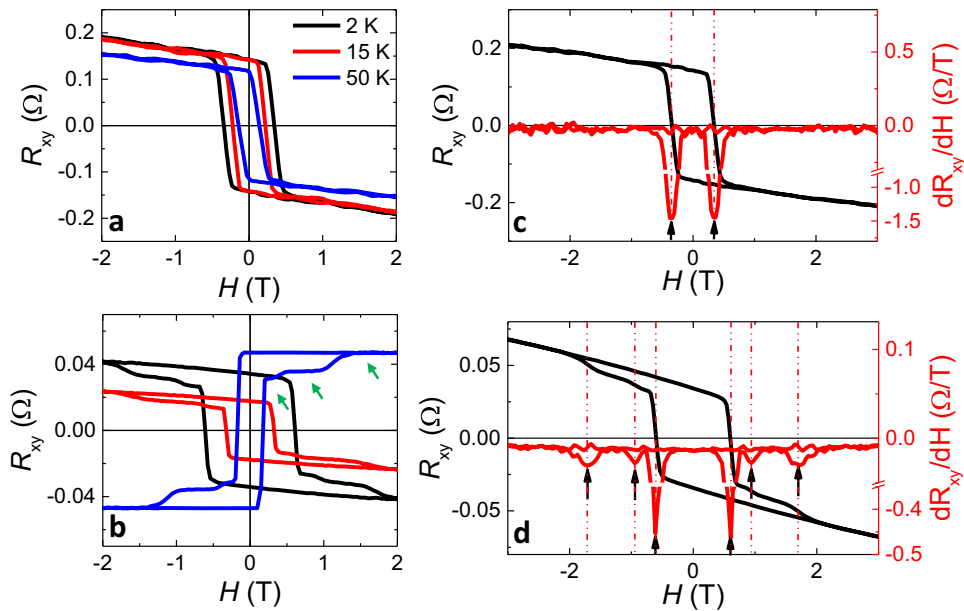


Fig. 2 Anomalous Hall effect in SRO films with controlled structural domains. Field-dependent Hall measured at different temperatures for (a) 75 u.c. SRO-15 and (b) 75 u.c. SRO-35. The first derivative of Hall versus field for (c) SRO-15 and (d) SRO-35. The temperature for Hall data is 2 K.

(X and Y) are observed for $\varphi \approx 35^\circ$ SRO film with the same thickness of 75 u.c., where both (100) and (010) facets are exposed and comparable due to serrated step edges (see Fig. 1e, f). Using their peak intensities, the volume ratio of X to Y-domain is estimated to be 2:1. For Y-domain, it is observed that (024) peak shifts rightward and (0–24) peak shifts leftward, suggesting that the unit cell of Y-domain tilts away from STO (001) plane, forming an inclined angle between Y-domain and STO (001) plane. This inclined angle is determined to be 0.02° (more details, see supplementary Fig. 5). In a scenario where X and Y-domain coexist, it is hard to directly identify the Z-domain since the $(44 \pm 4)_o$ from X and Y-domain fully overlap with $(\pm 2 \pm 28)_o$ from Z-domain. Note that structure factors for all $(44 \pm 4)_o$, $(260)_o$, and $(620)_o$ peaks are nearly identical. The fact that the peak intensity of $(44 \pm 4)_o$ is much lower than that of $(260)_o$ and $(620)_o$ implies certain destructive interference of Z-domain to the $(44 \pm 4)_o$ peaks and thus indicates a mixture of X, Y, and Z-domains in SRO-35 film (for more detail, see Supplementary Fig. 6). It is worth to note that the intensity of $(44 \pm 4)_o$ is only half of $(620)_o$ or $(260)_o$ for X-domain, hence the Z-domain has a very strong contribution to total peak intensity and its volume fraction is significant. The existence of Z-domain in this film is also indicated by transport and MFM measurements as we demonstrated in the following.

Impact of domain structure on anomalous Hall effect

Impacts of the domain formation on properties are demonstrated in Fig. 2. For SRO-15 with a single X-domain, the AHE shows a typical square-like hysteresis loop and a sharp sign change at coercive field (see Fig. 2a). In sharp contrast, the SRO-35 film with twin domains shows multiple switching, leading to three Hall plateaus as indicated by green arrows in Fig. 2b. The anomalous sign change of the Hall resistance with reducing temperature (e.g., 50 K vs. 15 K in Fig. 2b), which is commonly seen in SrRuO₃, is thought to arise from temperature-dependent Berry curvature in k-space driven by the change of band structure and magnetization^{24,36}. The single switching vs. multi-switching behaviors are better illustrated by the first derivative of Hall resistance as shown in Fig. 2c, d. For SRO-15, only a single peak at each side of the magnetic field (positive field and negative field) is observed, whereas there are three peaks exhibited by SRO-35 at each side.

Such miscut direction controlled switching in AHE is also observed in much thicker films, e.g., 250 u.c. (see Supplementary Fig. 7), indicating the long-range impact of step edge on domain formation.

Visualization of magnetic domains by MFM

In order to further reveal the relationship between the structural domains and magnetic domains, we performed the cryogenic MFM and in situ transport measurements in a Hall-bar geometry at various magnetic fields. Since the anisotropic field of SRO is extremely large, e.g., 12 T, the dipole–dipole interaction, which determines the magnetic domain structures in low-anisotropy materials, such as martensites³⁷, can be negligible in SRO. Therefore, the structurally pinned magnetic domains would follow local anisotropy and the magnetic domains can be mapped to structural domains. The single switching of SRO-15 sample was confirmed by MFM. The switching process was so sharp that it was very challenging for MFM technique to capture the magnetic domain boundaries. Occasionally, the long domain boundary ($>20 \mu\text{m}$) sweeping across the film could be captured by MFM (see Supplementary Fig. 8). This suggests that the SRO-15 film has a relatively small amount of magnetic disorder and thus exhibits a weak pinning effect. In sharp contrast, the magnetization reversal process of SRO-35, which has triple switching steps in Hall measurements, shows a much stronger pinning effect. During the first switching process, as shown in Fig. 3a–f, over 50% of the area was reversed. The reversed region is likely related to X-domain, since the first switching magnetic field is very close to the SRO-15 coercive field and X-domain has the largest volume fraction. The second switching process was also visualized in MFM images, as indicated by black circles in Fig. 3g, h. The remaining pinned area, which survived at higher magnetic fields up to 0.8 T, consisted of bubble-like domains with an average size around $1 \mu\text{m}$. Above 0.8 T, these magnetic bubbles were gradually reversed and the film was fully saturated at 1.6 T (see Fig. 3i–l). Via estimating the distribution of up and down domains, the M–H loop was estimated, as shown in Fig. 3m, which shows triple-step magnetic domain switching and thus is reasonably consistent with the Hall loop. The slight quantitative discrepancy is probably due to a spatial variation of structural twin domains over a length scale

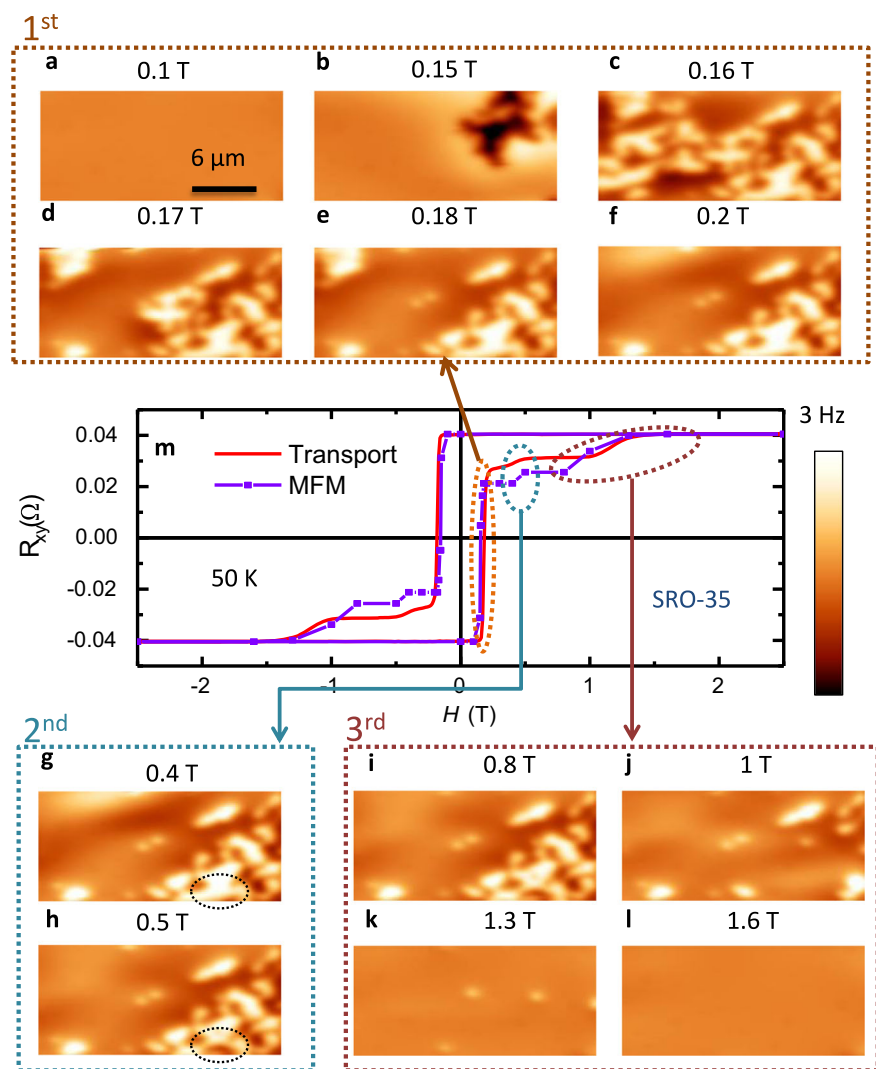


Fig. 3 Magnetization reversal in 75 u.c. SRO-35 film imaged by MFM. The magnetization reversal process exhibits triple-step behavior: **a–f** are the first step; **g, h** are the second step; **i–l** are the third step. **m** R_{xy} - H loop measured by transport (red) and estimated by distribution of up and down domains in MFM images (purple) shows similar behavior. The MFM images were taken at 50 K.

much larger than the scan size ($\sim 20 \times 20 \mu\text{m}^2$) of our MFM. The discrepancy could be reduced by sampling a larger area.

To further confirm the fact that structural domains pin the ferromagnetic domains, especially the minor Z or Y-domain in the film, which are hard to be investigated separately, we performed the MFM studies on a 250 u.c. SRO-30 sample, which was comprised of only X and Z-domains (see Supplementary Fig. 9). The Hall resistance of SRO-30 sample exhibited two-step switching, in good agreement with two types of structural domains. The volume percentage of Z and X-domain is quantified by the RSMs data. The ratio of Z to X-domain is around 0.12:1, which agrees with the ratio of two-step sizes in the anomalous Hall data ($\sim 0.1:1$), suggesting again the correlation between magnetic and structural domains. Field-dependent MFM images taken on this 250 u.c. film also confirm this relationship. As shown in Fig. 4a–e, the majority of the film has been reversed during the first switching process, which is related to X-domain. Scattered magnetic bubble domains which remained at higher fields around 1.1 T and were entirely switched at 1.4 T then are assigned to the Z-domain (see Fig. 4f–i). This is further evidenced by the fact that the M–H loop estimated by MFM is quantitatively consistent with Hall loop as shown in Fig. 4j and also the fact that the isolated small bubble occupies nearly 10% volume fraction. Comparing the three domains and

their switching fields in 75 u.c. SRO-35 with those in 250 u.c. SRO-30, we can conclude that (1) the regions with low switching field in SRO-35 are X-domain; (2) the regions with high switching field are Z-domain; (3) the rest with intermediate switching field are Y-domain. The field loop measurement of the MFM images directly confirms the pinning of the magnetic domains (see Supplementary Fig. 10), further indicating one-to-one corresponding between structural domains and magnetic domains. We also notice that the domains are irregular, which are similar with previously reported domain structures revealed microscopically by transmission electron microscopy^{32,38}. This irregular shape of domains may arise from complex interplay between domain wall energy, miscut direction, and thermal dynamics during growth. The agreements between x-ray RSMs, transport and MFM data demonstrate that the multiple-step behavior in the magnetic reversal process is intimately related to the populations of structural domains.

Origin of multi-step switching

The multiple-step switching shown in Hall resistance and magnetization data is a result of domain-dependent coercive fields. The orthorhombic SRO films, regardless of the type of domains, exhibit uniaxial magnetocrystalline anisotropy. Experiments on twin free (110)_o orientated SRO films indicated that the

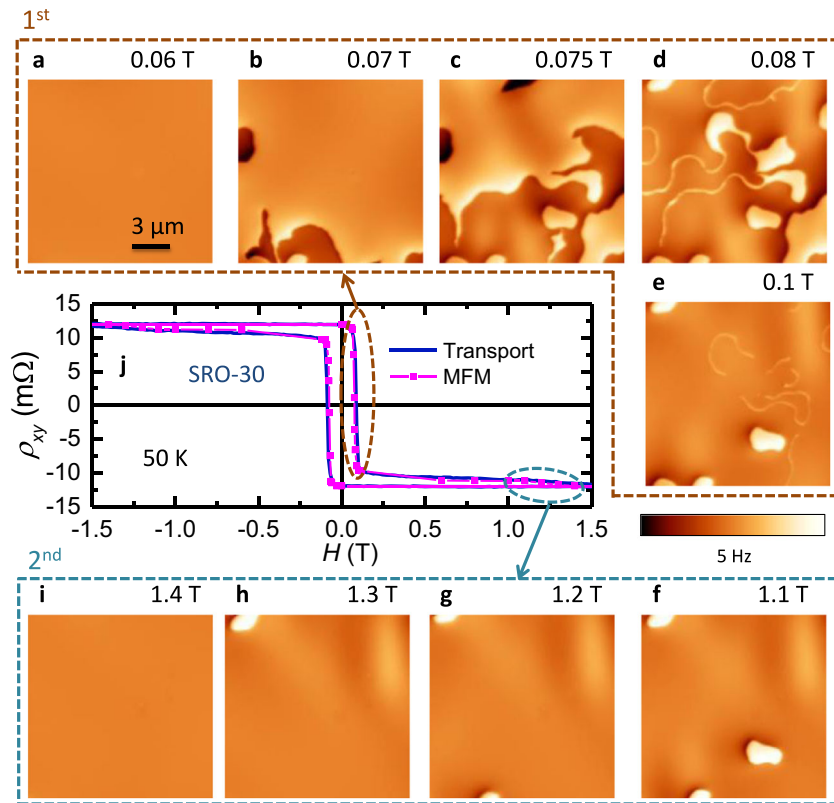


Fig. 4 Magnetization reversal in 250 u.c. SRO-30 film imaged by MFM. The magnetization reversal process exhibits two-step behavior: **a–e** is the first step; **f–i** is the second step. **j** Field-dependent Hall resistance measured by transport (blue) at 50 K and that estimated by MFM images (magenta) show similar behavior. The MFM images were taken at 50 K.

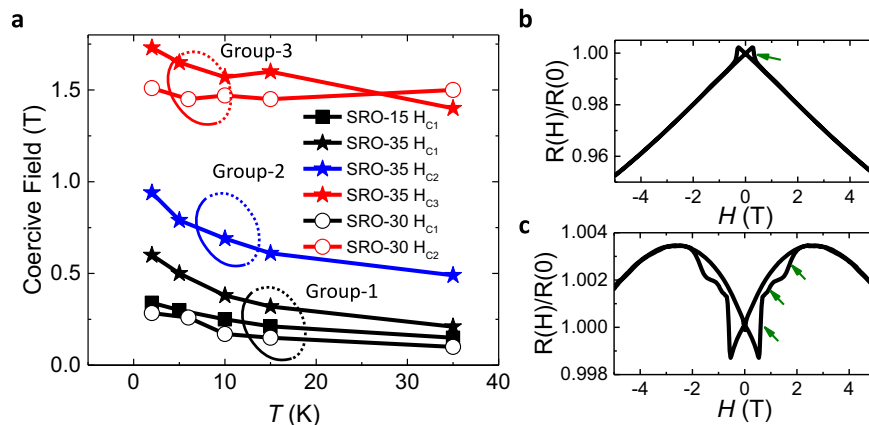


Fig. 5 Categorization of coercive fields and sign change in magnetoresistance. **a** The temperature-dependent coercive field determined from Hall measurement. The magnetoresistance of **(b)** SRO-15 and **(c)** SRO-35. The thicknesses of SRO-15 and SRO-35 are 75 u.c. and thickness of SRO-30 is 250 u.c.

easy axis lies in $(001)_o$ plane and points at $\sim 30^\circ$ relative to $[110]_o$ direction at low temperature^{24,39,40}. Prior Lorentz TEM studies showed that the easy axis is close to $[100]_o$, which is the long axis of ab plane, irrespective of the type of domains⁴¹. It has been further found that the easy axis orientation is sensitive to the variation of rotation and tilt of RuO_6 octahedra¹³. For Z-domain, the easy axis lies closer to in-plane direction, leading to an out-of-plane hard axis and a much bigger coercive field than X or Y-domain. The temperature-dependent coercive fields are shown in Fig. 5a. The coercive fields are obtained from the peaks in dR_{xy}/dH vs. H curves as illustrated in Fig. 2. For SRO-15, there is only one coercive field from single X-domain, while for SRO-35, three

coercive fields arise from X, Y, and Z-domain, respectively. With respect to SRO-30, two coercive fields from X and Z-domain are observed. Comparing these values, the coercive fields can be categorized into three groups (H_{C1} , H_{C2} , and H_{C3}) as indicated by black, blue and red circles in Fig. 5a. The group-1 which has the lowest coercive field is attributed to X-domain. The group-3, which has the largest value, is attributed to Z-domain as illustrated from SRO-30 sample. In between is the group-2, which is then attributed to the remaining tilted Y-domain. The Y-domain though is also (110) orientated, it tilts away from STO (001) , which as a result will lead to different structure distortion from nontilted X-domain due to different interface structure coupling effect.¹³

Additionally, the size of *Y*-domain is much smaller than *X*-domain (see Fig. 3). The *X*-domain can create a vertical interface with *Y*-domain and thus can modify the structure of *Y*-domain as well. The different structure distortion and smaller domain size than *X*-domain could explain the slightly bigger coercive field of *Y*-domain than *X*-domain. Quantitative understanding of the unit tilting effect on magnetic anisotropy will require further investigation. The slightly different structure and coercive field between *X* and *Y*-domain could cause a little discrepancy of domain ratio estimated from RSMs than that estimated from AHE data and MFM image shown in Fig. 3m. Partial *Y*-domain could be dragged by already switched *X*-domain and switched earlier before H_{C2} , leading to an underestimated *Y* to *X*-domain ratio. Note that the coercive field of 75 u.c. SRO-35 is higher than those of 250 u.c. SRO-30 and 75 u.c. SRO-15 in each sub-group, likely due to the smaller domain size in SRO-35.

Impact of domain formation on magnetoresistance

The domain formation is found to fundamentally change the magnetoresistance. Typical negative magnetoresistance arising from the suppression of spin fluctuation⁴² is observed in SRO-15 and the hysteresis loop is caused by ferromagnetic domain reversal (see Fig. 5b and Supplementary Fig. 11). Differently, the SRO-35 shows positive MR at low-field (<2.6 T) and triple-step switching (see Fig. 5c). This positive MR feature is also seen in Hall-bar geometry with $I//[100]$ (see Supplementary Fig. 12). The low-field positive MR could arise from *Z*-domain. As reported by Gunnarsson et al., positive MR arises when field is parallel to $[001]_o$ direction³⁴, which has been suggested to originate from antilocalization effect or anisotropic magnetoresistance owing to relatively large spin-orbit coupling in SRO. Therefore, the *Z*-domain whose $[001]_o$ is along out-of-plane direction then will produce positive MR. For SRO-35, it contains ~14% of *Z*-domain as estimated from AHE data (see Fig. 2b). The existence of *Z*-domain correlates with low-field positive MR. The triple-step switching in MR for SRO-35 should arise from magnetic domain wall resistance. Since different structurally pinned magnetic domains have different coercive fields, the magnetic domain reversal process will induce magnetic domain walls and thus domain wall resistance.

DISCUSSION

In summary, the geometric control of domain formation and physical properties are demonstrated in SRO thin films grown on (001) STO. Structurally twin free and twinned SRO films can be deliberately controlled by substrate miscut direction. Using cryogenic MFM to visualize the domain behavior in magnetization reversal process, we show that the local coercive fields correlate with the orthorhombic twin domains. This correlation leads to multiple magnetization switching steps in multi-twin-domain SRO films. More interestingly, introducing the $[001]_o$ domain (*Z*-domain) results in positive low-field magnetoresistance, which is otherwise absent. The demonstration of a close link between magnetic domains and structural twin domains provides deep insight into the domain formation and its importance in determining physics properties. The controlled domain formation by tuning substrate miscut geometry also implies an additional avenue toward rational materials design for desired functionalities in future spintronic applications.

METHOD

Thin-film synthesis and characterization

The SrRuO₃ (SRO) thin films were epitaxially grown on TiO₂ terminated (001) STO substrates using PLD technique. The single TiO₂ terminated STO substrates were achieved by standard buffer HF etching for 30 s and

subsequent annealing at 950 °C for 90 min. The substrate temperature and oxygen partial pressure during growth were 650 °C and 0.25 mBar, respectively. The laser fluence and repetition rate were 2 J/cm² and 1 Hz, respectively. In situ RHEED was used to monitor the growth. The substrates and films surface morphology was characterized by atomic force microscopy (AFM). Lattice structure of the films was characterized by PANalytical X'Pert Materials Research Diffractometer in high resolution mode.

Transport and magnetic properties measurement

The Hall resistance and magnetoresistance were measured by Quantum Design Physical Property Measurement System using van der Pauw method. All the Hall data were antisymmetrized.

MFM and in situ transport measurement

The MFM experiments were performed in an in-house-built cryogenic AFM. The tips for the MFM were coated by a nominally 100 nm Co film using e-beam evaporation. MFM images were taken in a constant-height mode with the scanning plane ~80 nm above the sample surface. To avoid the relaxation effect (domain wall creeping) near H_C and to minimize the stray field effect of the MFM tips, all MFM images were taken at a low magnetic field of ~0.05 T after the magnetic field was ramped to the desired values. The MFM signal, the change of cantilever resonant frequency, is proportional to the out-of-plane stray field gradient. Electrostatic interaction was minimized by nulling the tip-surface contact potential difference. Dark (bright) regions in the MFM images represent up (down) ferromagnetic domains, where magnetizations are parallel (antiparallel) with respect to the positive external field. The in situ Hall resistance and longitudinal resistance were measured in a Hall-bar geometry by standard lock-in techniques with an alternating current of 40 μA modulated at 314 Hz. All Hall data were antisymmetrized.

DATA AVAILABILITY

The data that support the findings of this study are available from the corresponding author upon reasonable request.

Received: 2 June 2020; Accepted: 24 September 2020;

Published online: 16 October 2020

REFERENCES

1. Hwang, H. Y. et al. Emergent phenomena at oxide interfaces. *Nat. Mater.* **11**, 103–113 (2012).
2. Huang, Z. et al. Interface engineering and emergent phenomena in oxide heterostructures. *Adv. Mater.* **30**, 1802439 (2018).
3. Zubko, P. et al. Interface physics in complex oxide heterostructures. *Annu. Rev. Condens. Matter Phys.* **2**, 141–165 (2011).
4. Ohtomo, A. & Hwang, H. Y. A high-mobility electron gas at the LaAlO₃/SrTiO₃ heterointerface. *Nature* **427**, 423–426 (2004).
5. Lee, H. et al. Direct observation of a two-dimensional hole gas at oxide interfaces. *Nat. Mater.* **17**, 231–236 (2018).
6. Das, S. et al. Observation of room-temperature polar skyrmions. *Nature* **568**, 368–372 (2019).
7. Wang, W. et al. Spin chirality fluctuation in two-dimensional ferromagnets with perpendicular magnetic anisotropy. *Nat. Mater.* **18**, 1054–1059 (2019).
8. Li, D. et al. Superconductivity in an infinite-layer nickelate. *Nature* **572**, 624–627 (2019).
9. Choi, K. J. et al. Enhancement of ferroelectricity in strained BaTiO₃ thin films. *Science* **306**, 1005–1009 (2004).
10. Schlom, D. G. et al. Strain tuning of ferroelectric thin films. *Ann. Rev. Mater. Res.* **37**, 589–626 (2007).
11. Ward, T. Z. et al. Elastically driven anisotropic percolation in electronic phase-separated manganites. *Nat. Phys.* **5**, 885–888 (2009).
12. Liao, Z. et al. Controlled lateral anisotropy in correlated manganite heterostructures by interface-engineered oxygen octahedral coupling. *Nat. Mater.* **15**, 425–431 (2016).
13. Kan, D. et al. Tuning magnetic anisotropy by interfacially engineering the oxygen coordination environment in a transition metal oxide. *Nat. Mater.* **15**, 432–437 (2016).
14. Kim, T. H. et al. Polar metals by geometric design. *Nature* **533**, 68–72 (2016).

15. Glazer, A. The classification of tilted octahedra in perovskites. *Acta Crystallogr. Sect. B* **28**, 3384–3392 (1972).
16. Kalisky, B. et al. Locally enhanced conductivity due to the tetragonal domain structure in LaAlO₃/SrTiO₃ heterointerfaces. *Nat. Mater.* **12**, 1091–1095 (2013).
17. Guo, E.-J. et al. Nanoscale ferroelastic twins formed in strained LaCoO₃ films. *Sci. Adv.* **5**, eaav5050 (2019).
18. Van Aert, S. et al. Direct observation of ferroelectricity at ferroelastic domain boundaries in CaTiO₃ by electron microscopy. *Adv. Mater.* **24**, 523–527 (2012).
19. Liao, Z. et al. Long-range domain structure and symmetry engineering by interfacial oxygen octahedral coupling at heterostructure interface. *Adv. Funct. Mater.* **26**, 6627–6634 (2016).
20. Huijben, M., Koster, G., Liao, Z. L. & Rijnders, G. Interface-engineered oxygen octahedral coupling in manganite heterostructures. *Appl. Phys. Rev.* **4**, 041103 (2017).
21. Frenkel, Y. et al. Imaging and tuning polarity at SrTiO₃ domain walls. *Nat. Mater.* **16**, 1203–1208 (2017).
22. Rojac, T. et al. Domain-wall conduction in ferroelectric BiFeO₃ controlled by accumulation of charged defects. *Nat. Mater.* **16**, 322–327 (2016).
23. Mundy, J. A. et al. Functional electronic inversion layers at ferroelectric domain walls. *Nat. Mater.* **16**, 622–627 (2017).
24. Koster, G. et al. Structure, physical properties, and applications of SrRuO₃ thin films. *Rev. Mod. Phys.* **84**, 253–298 (2012).
25. Matsuno, J. et al. Interface-driven topological Hall effect in SrRuO₃-SrIrO₃ bilayer. *Sci. Adv.* **2**, e1600304 (2016).
26. Qin, Q. et al. Emergence of topological Hall effect in a SrRuO₃ single layer. *Adv. Mater.* **31**, 1807008 (2019).
27. Meng, K.-Y. et al. Observation of nanoscale skyrmions in SrIrO₃/SrRuO₃ bilayers. *Nano Lett.* **19**, 3169–3175 (2019).
28. Wang, L. et al. Ferroelectrically tunable magnetic skyrmions in ultrathin oxide heterostructures. *Nat. Mater.* **17**, 1087–1094 (2018).
29. Jones, C. W., Battle, P. D., Lightfoot, P. & Harrison, W. T. A. The structure of SrRuO₃ by time-of-flight neutron powder diffraction. *Acta Crystallogr. Sect. C* **45**, 365–367 (1989).
30. Wang, L. et al. Controllable thickness inhomogeneity and Berry curvature engineering of anomalous Hall effect in SrRuO₃ ultrathin films. *Nano Lett.* **20**, 2468–2477 (2020).
31. Lu, W. et al. Control of oxygen octahedral rotations and physical properties in SrRuO₃ films. *Phys. Rev. B* **88**, 214115 (2013).
32. Jiang, J. C. et al. Domain structure of epitaxial SrRuO₃ thin films on miscut (001) SrTiO₃ substrates. *Appl. Phys. Lett.* **72**, 2963–2965 (1998).
33. Klein, L. et al. Transport and magnetization in the badly metallic itinerant ferromagnet. *J. Phys.: Condens. Matter* **8**, 10111–10126 (1996).
34. Gunnarsson, R. Anisotropic spin-orbit interaction revealed by in-plane magnetoresistance in single-oriented SrRuO₃ thin films. *Phys. Rev. B* **85**, 235409 (2012).
35. Vaillonis, A., Siemons, W. & Koster, G. Strain-induced single-domain growth of epitaxial SrRuO₃ layers on SrTiO₃: a high-temperature x-ray diffraction study. *Appl. Phys. Lett.* **91**, 071907 (2007).
36. Fang, Z. et al. The anomalous Hall effect and magnetic monopoles in momentum space. *Science* **302**, 92–95 (2003).
37. Golub, V. et al. Magnetism of nanotwinned martensite in magnetic shape memory alloys. *J. Phys.: Condens. Matter* **32**, 313001 (2020).
38. Jiang, J. C., Pan, X. Q., Gan, Q. & Eom, C. B. Domain structure of epitaxial SrRuO₃ thin films on (001) LaAlO₃. *Microsc. Microanal.* **4**, 578–579 (1998).
39. Yoo, Y. Z. et al. Diverse effects of two-dimensional and step flow growth mode induced microstructures on the magnetic anisotropies of SrRuO₃ thin films. *Appl. Phys. Lett.* **89**, 124104 (2006).
40. Ziese, M., Vrejoiu, I. & Hesse, D. Structural symmetry and magnetocrystalline anisotropy of SrRuO₃ films on SrTiO₃. *Phys. Rev. B* **81**, 184418 (2010).
41. Marshall, A. F. et al. Lorentz transmission electron microscope study of ferromagnetic domain walls in SrRuO₃: Statics, dynamics, and crystal structure correlation. *J. Appl. Phys.* **85**, 4131–4140 (1999).
42. Gausepohl, S. C. et al. Magnetoresistance properties of thin films of the metallic oxide ferromagnet SrRuO₃. *Phys. Rev. B* **52**, 3459–3465 (1995).

ACKNOWLEDGEMENTS

The work at USTC was financially supported by National Nature Science Foundation of China (11974325), Hundred Talent Program of the Chinese Academy of Sciences (KJ231000010) and the Fundamental Research Funds for the Central Universities (2019HSC-CIP008). The work at Rutgers was supported by the Office of Basic Energy Sciences, Division of Materials Sciences and Engineering, US Department of Energy under Award numbers DE-SC0018153.

AUTHOR CONTRIBUTIONS

W.W. performed the MFM and transport measurement. L.L., J.L., B.C., Y.J., G.C., Y.L., G.K., G.R., and Z.L. synthesized the samples and performed transport measurement. L.L., B.C., G.K., G.R., and Z.L. performed the XRD measurement. W.W., W.Wu, and Z.L. wrote the paper. All authors discussed the data and contributed to the paper.

COMPETING INTERESTS

The authors declare no competing interests.

ADDITIONAL INFORMATION

Supplementary information is available for this paper at <https://doi.org/10.1038/s41535-020-00275-5>.

Correspondence and requests for materials should be addressed to Z.L.

Reprints and permission information is available at <http://www.nature.com/reprints>

Publisher's note Springer Nature remains neutral with regard to jurisdictional claims in published maps and institutional affiliations.



Open Access This article is licensed under a Creative Commons Attribution 4.0 International License, which permits use, sharing, adaptation, distribution and reproduction in any medium or format, as long as you give appropriate credit to the original author(s) and the source, provide a link to the Creative Commons license, and indicate if changes were made. The images or other third party material in this article are included in the article's Creative Commons license, unless indicated otherwise in a credit line to the material. If material is not included in the article's Creative Commons license and your intended use is not permitted by statutory regulation or exceeds the permitted use, you will need to obtain permission directly from the copyright holder. To view a copy of this license, visit <http://creativecommons.org/licenses/by/4.0/>.

© The Author(s) 2020